Spontaneous Formation of Heterodimer Au-Fe_7S_8 Nanoplatelets by a Seeded Growth Approach

Shaghraf Javaid [†], *Yunguo Li* [‡], *Dechao Chen*[†], *Xiaomin Xu*[§], *Yingping Pang*[†], *Wei Chen*[†], *Fei Wang*[†], *Zongping Shao*[§], *Martin Saunders*[‖], *Jean-Pierre Veder*[⊥], *Guohua Jia*[†*], *Franca Jones*[†*]

[†] Curtin Institute of Functional Molecules and Interfaces, School of Molecular and Life Science, Curtin University, Bentley WA 6102, Australia

[‡] Faculty of Mathematical and Physical Sciences, University College London, Gower Street, London WC1E 6BT, United Kingdom

[§] Department of Chemical Engineering, Curtin University, Bentley WA 6102, Australia

[‖] Centre for Microscopy, Characterization and Analysis (CMCA) and School of Molecular Sciences, The University of Western Australia, Crawley, WA 6009, Australia

[⊥] John de Laeter Centre, Curtin University, Bentley WA 6102, Australia

[*] Corresponding author: guohua.jia@curtin.edu.au; F.Jones@curtin.edu.au;

ABSTRACT:

Hybrid nanomaterials offer increased flexibility to achieve heterostructures with controlled functionalities and predictable linkages owing to their synergistic interactions. Here, we have developed a synthetic strategy that produced hexagonal-shaped nanoplatelets (NPLs) of gold-pyrrhotite (Au-Fe_7S_8) with Au embedded inside them by means of a seeded growth method. By using thiol-capped Au nanoparticles (NPs) as a seed, heterogeneous nucleation of the iron precursor was facilitated, leading to the formation of Au-Fe_7S_8 NPLs. The injection temperature and surface ligand of the seed (Au) were two critical factors that determined the homogeneity and final morphology of the Au-Fe_7S_8 NPLs. This strategy was further expanded using Ag NPs as the seed to construct heterodimers, producing Ag_2S-Fe_7S_8 heterostructures.

INTRODUCTION:

Nanoscale engineering has provided new means of control over the composition, morphology and properties of a wide range of materials. Typically, materials with multiple domains coupled together are of primary interest to obtain tunable and multifunctional targets with enhanced properties. These heterostructures are regarded as hybrid nanomaterials and can facilitate applications in number of fields in such a way that are not achievable with bulk materials.[1-9] Recently, transition metal sulfides have attracted research interest for various energy storage applications such as electrocatalysis, coating of photogalvanic cells, electrode materials for lithium ion batteries and supercapacitors.[10-12] Among other metal sulfides, iron sulfides are an important component of magnetic chalcogenides with some significant properties but have not been explored much compared to their counterparts i.e. iron oxides. This can be attributed to the complex stoichiometric ratio between iron and sulfide ion, the high affinity of iron with oxygen

(which makes it hard to prevent oxide and hydroxide impurities) and the phase change sensitivity towards reaction temperature.[13-17]

Pyrrhotite (Fe_7S_8) is one of the many stoichiometric forms of iron sulfide and is an attractive candidate for electrocatalytic applications and as an anode material for lithium-sodium ion batteries.[18-20] Despite its potential, this material has not been investigated much. Only few attempts have been made where Fe_7S_8 was laminated,[19] doped,[21] partially and completely cation exchanged[22] with another material to attain hybrid heterogeneous structure but even this study still lacked a systematic synthesis approach. Since last decade, multiple noble metal-iron oxide based hybrid heterodimers and trimers have been reported. For example, Schaak's group has successfully shown the construction of high order hybrid materials i.e. dimers (Au-Fe_3O_4, PtPb-Fe_3O_4, $PtSn_3Fe_3O_4$)[23,24], trimers (M-Pt-Fe_3O_4; M = Au, Ag, Ni, Pd, Au-Ge-Fe_3O_4)[23, 25] and tetramers (M_xS-Au-Pt-Fe_3O_4; M= Pb & Cu)[25]. These examples highlight the prospect of obtaining sophisticated noble metal based heterostructures of iron sulfides.

A careful consideration of the synthesis approach is mandatory for the rational combination of distinct entities. The selected approach must facilitate the formation of every individual material at a precise location within the heterostructures. Based on extensive research, the heterogeneous seeded-growth method is the most appropriate one for the synthesis of hybrid heterodimers.[23] Here one domain is used as a seed which stimulates the heterogeneous nucleation of another one on it reinforcing the crucial dependence of this method on the active sites of the seed's surface. Attention must be paid to suppress homogeneous nucleation which can be overcome by choosing appropriate capping agents.[8, 26-29].

In this contribution, we report unique hexagonal shaped hybridized heterodimer nanoplatelets (NPLs) of Au-Fe_7S_8, a new material. In this nanostructure, a central role was played by the seed particles (Au, Ag) functionalized by a ligand, 1-dodecanethiol (DDT),[30] which also actively acted as a sulfur source for the second domain (Fe_7S_8) and consequently led to its growth only on the surface of the seed. It should be noted here that thiol (–SH) deprotonates resulting in the formation of –S-Au NP seeds [31] and therefore in further discussion these thiol derivatised Au NPs will be referred to as thiol capped Au NPs. This approach allowed us to eliminate homogenous nucleation and accomplish our goal of getting well-defined hexagonal shaped NPLs with Au seed embedded at the center. Due to the magnetic nature of Fe_7S_8, a strong response was seen towards an external magnetic field which brought the benefit of magnetic separation.

In this study, we have also presented experimental evidence for the existence of a strong relation between the final morphology of our heterodimer with the temperature at which the seed (Au) is injected into the reaction mixture. To the best of our knowledge, this is the first time that hybrid NPLs for the pyrrhotite family have been reported which provides an exciting opportunity to explore such unique heterostructures with different combinations of noble metals and iron sulfides for potential applications in catalysis.[18]

EXPERIMENTAL SECTION:

Materials. Hydrogen tetrachloroaurate (III) trihydrate ($HAuCl_4.3H_2O$) (99.9%), sodium borohydride ($NaBH_4$) (≥98%), n-tetraoctylammonium bromide (n-Oct_4NBr) (98%), 1-dodecanethiol (DDT) (≥98%), hexadecanethiol (HDT) (≥95%), octadecanethiol (ODT) (98 %), iron (III) acetylacetonate $Fe(acac)_3$ (99.9%), silver acetylacetonate (Ag(acac)) (99%), 1-octadecene (ODE) (technical grade 90%), oleic acid (OA) (technical grade 90%), oleylamine

(OL-Am) (97%) were purchased from Sigma Aldrich. All chemicals were used as received without further purification.

Synthesis of Au NPs by Brust method. A 20 ml aqueous solution of $HAuCl_4$ (5 mM) was mixed with 10 ml of n-Oct_4NBr (25 mM) in toluene. It was left for a few minutes before separating the organic phase and adding 259 μL of DDT. A freshly prepared aqueous solution of 0.054 g $NaBH_4$ in 3 ml of water was added into the organic phase under vigorous stirring. There was an instant change in colour from a clear to dark brown solution indicating the formation of Au NPs. After further stirring for 1 hr, Au NPs were precipitated with ethanol and dispersed in hexane. From this procedure, Au NPs of 1-3 nm in size were obtained as confirmed by transmission electron microscopy (TEM, Figure S1 (a) inset). HDT and ODT capped Au NPs were prepared in a similar manner with HDT or ODT replacing the DDT.

Synthesis of Au NPs using the Oleylamine method. To synthesize oleylamine capped Au NPs, 100 mg of $HAuCl_4$ was mixed with 10 ml of oleylamine and toluene respectively in a 50 ml three-neck round bottom flask. The reaction mixture was filled with nitrogen via a Schlenk line system and the temperature was raised gradually to up to 120 °C. The reaction mixture was kept at this temperature for 45 mins during which its colour changed to wine red. The product was cooled to room temperature followed by isolation of the particles with ethanol (1:1 by v/v) before finally dispersing in hexane. From this procedure, Au NPs of 5-7 nm in size were obtained as confirmed by TEM (Figure S2 (a) inset).

Synthesis of Au-Fe_7S_8 NPLs. For the synthesis of a heterodimer of Au-Fe_7S_8, 68.5 mg of $Fe(acac)_3$ was dissolved in 20 ml of ODE and 1 ml of OA in a 50 ml three-necked round bottom flask equipped with a temperature adapter, reflux condenser and rubber septum. To ensure the

complete removal of low boiling point constituents, the solution was first degassed at 70 °C and was then held at 110 °C under vacuum for 90 mins to generate the iron oleate precursor *in-situ*. Meanwhile, in a separate flask a solution containing 2 ml (5 mg) of the Au NPs (from the Brust method) dispersed in hexane (from the Brust method), 2 ml of ODE and 1 ml of oleylamine was degassed under vacuum at room temperature. After 30 mins, 150 µL of DDT was injected into the same solution under a nitrogen blanket and was kept under these conditions for another 30 mins. To get the heterodimer of Au-Fe_7S_8 via heterogeneous nucleation, the aforementioned Au NPs solution were injected into the iron precursor solution at 160 °C under inert atmosphere. At this stage a significant colour change was observed from orange-red to deep brown. The reaction mixture was then heated to up to 280 °C and kept at this temperature for another 20 mins, allowing the complete nucleation and growth of Fe_7S_8 on the Au NPs domain. Apart from acting as a surface stabilizer, OL-Am in the reaction mixture also participates in an aminolytic reaction which results in the formation of water vapour. This could sometimes result in bumping of the reaction, making it difficult to maintain the desired temperature. The final product was isolated by the addition of excess ethanol followed by centrifugation at 6800 rpm for 3 mins. The precipitated NPs were re-dispersed in hexane and washed repeatedly with ethanol/hexane (1:4 v/v) until clear supernatant liquid is obtained. Finally, the obtained NPs were redispersed into hexane and transferred to a vial for storage. The same experimental conditions were used for the synthesis of Au-Fe_7S_8 NPLs with HDT and ODT capped Au NPs.

Effect of injection temperature. The effect of temperature at which the Au NPs were injected into the iron precursor solution was investigated. To reveal the influence of temperature on the heterogeneous nucleation and final morphology of the iron sulfide NPLs, Au NPs were injected into the reaction mixture at 110, 120, 140, 160, 180, 200, 220, 240, 260 and 280 °C. As

mentioned above, the reaction mixture was heated up to a final temperature of 280 °C and was kept at the same temperature for 20 mins. All other reaction parameters were kept constant.

Synthesis of thiol capped Ag NPs. To synthesize thiol capped Ag NPs, 22.7 mg of Ag(acac) was mixed with 4.38 ml of DDT. This reaction mixture was degassed at room temperature followed by a nitrogen blanket. The temperature was gradually raised to 220 °C and left at this temperature for 15 mins. Precipitates were isolated by the addition of excess acetone followed by re-dispersion in hexane.

Synthesis of Ag_2S-Fe_7S_8. The experimental procedure for the synthesis Ag_2S-Fe_7S_8 was similar to that described above for the synthesis of Au-Fe_7S_8, except that DDT capped silver nanoparticles were used as the seeds with 300 μL of DDT (rather than the Au NPs with 150 μL of additional DDT).

Characterization. Transmission electron microscopy (TEM) images and selected area electron diffraction (SAED) were collected on a JOEL 2100 at the University of Western Australia and on a FEI Talos F200X-FEG-TEM at the John de laeter centre, Curtin University. High resolution TEM (HRTEM) images, fast fourier transform (FFT) patterns, high angle annular dark field-scanning TEM (HAADF-STEM), elemental mapping and energy dispersive X-ray spectroscopy (EDS) were obtained on a FEI Titan G2 80-200 high resolution transmission electron microscope. The powder X-ray diffraction (XRD) pattern was collected on a D8 Advance (Bruker AXS, Germany) with Cu Kα radiation source at 40 KV/40 mA with a LynxEye detector. X-ray photoelectron spectroscopy (XPS) measurements were performed on a Kratos AXIS Ultra DLD (see Supporting Information for more details) at the John de laeter Centre, Curtin University. Thermal gravimetric analysis was done on a TA instruments SDT Q600 in nitrogen

atmosphere with a flow rate of 100 ml/min while UV-Vis spectra were obtained on a Perkin Elmer Lambda 35 UV-VIS spectrometer after diluting the sample with hexane. Atomic force microscope (AFM) images were obtained on a Bruker Dimension Icon AFM. Particle sizing was determined by measuring more than 100 particles per sample.

RESULTS AND DISCUSSION

Formation of Au-Fe_7S_8 NPLs. Herein, we report the synthesis of Au-Fe_7S_8 NPLs by means of a typical heterogeneous seeded-nucleation method. First, $Fe(acac)_3$was used as an Fe (III) precursor in the presence of OA and OL-Am. Here, OA is believed to make an *in-situ* complex of iron oleate [$Fe(C_{18}H_{34}O_2)_3$] which then decomposes by OL-Am at elevated temperatures via an aminolysis reaction.[21] Both OL-Am and residual OA also acted as a surface stabilizing agents. As mentioned above, thiol-capped Au NP (see S1, inset) seeds were injected into the iron precursor solution at 160 °C followed by ramping up the temperature to 280 °C. We believe that at elevated temperatures, the iron precursor starts reacting with the thiol ligand immobilized on the surface of Au seeds to initiate the formation of iron sulfide around it. Under normal circumstances homogeneous nucleation and agglomeration of Au and Fe_7S_8 could also occur separately, however, the surface ligand stops this from occurring and leads to heterogeneous nucleation. As a result of this key interaction between the iron, Au NPs seeds and the thiol containing ligand (DDT) we observed the formation of hexagonal shaped hybrid NPLs (Au-Fe_7S_8). Figure 1 presents a schematics of the evolution of pyrrhotite NPLs at different temperatures and also illustrates the uniqueness of our work which lies in the controlled utilization of the thiol ligand on the surface of Au NPs rather than adding any extra sulfur source.

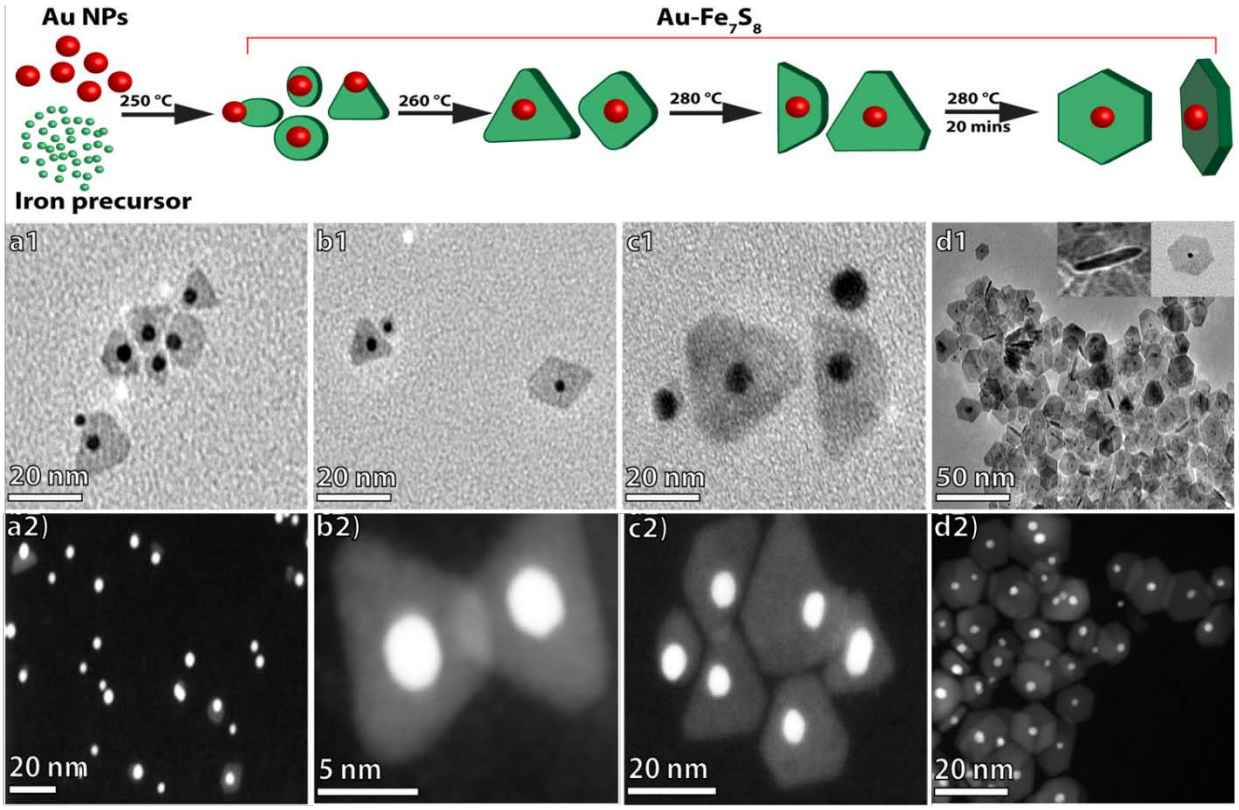

Figure 1: Stepwise schematic representation of the formation of hybrid hexagonal shaped heterodimers of Au-Fe_7S_8 along with the temperatures and reaction time. Representative TEM and HAADF-STEM images of the aliquots show Au-Fe_7S_8 at (a1-a2) 250°, (b1-b2) 260°, (c1-c2) 280° and (d1-d2) 280 °C after 20 mins.

Evolution of monoclinic heterostructures. TEM and HAADF-STEM images in Figure 1 a-d illustrate the mechanistic evolution of the hybrid heterodimer of Au-Fe_7S_8 from irregular triangular (250 °C) structures to regular and well-defined hexagonal-shaped (280 °C) NPLs. It also highlights the rapid growth of pyrrhotite within the short temperature range of 250-280 °C, forming a monoclinic structure at 280 °C after 20 mins with Au seed embedded inside it (Figure 1 d1 inset, Figure S1). This evolution of Au-Fe_7S_8 heterodimer was observed not only in terms of shape but also in size as shown in the size distribution curve (Figure S3). No substantial

growth of iron sulfide was observed on the seed surface at a temperature lower than 250 °C. These observations suggest that iron uses sulfur from the thiol stabilized Au NPs (-S-Au) as the sulfur source, whilst promoting heterogeneous nucleation, only at a temperature higher than 250 °C for the formation of Fe_7S_8 NPLs. So, during the course of the reaction, aliquots were obtained at different reaction temperatures and some of the representative TEM (Figure 1a1-d1) and HAADF-STEM (Figure 1a2-d2) images are provided in Figure 1.

Effect of injection temperature of the seed (Au NPs). The evolution of these dimers (Au-Fe_7S_8) into perfect hexagonal-shaped NPLs was observed only when Au NPs were injected at a low temperature, i.e. below 180 °C. To determine the effect of the seeds injection temperature on the crystallinity and shape of the final product, we conducted several parallel experiments where Au NPs were injected within a temperature range of 110-280 °C. Figure 2 presents the TEM images of the final heterodimers that were obtained when changing the seeds injection temperature whilst keeping other reaction parameters constant.

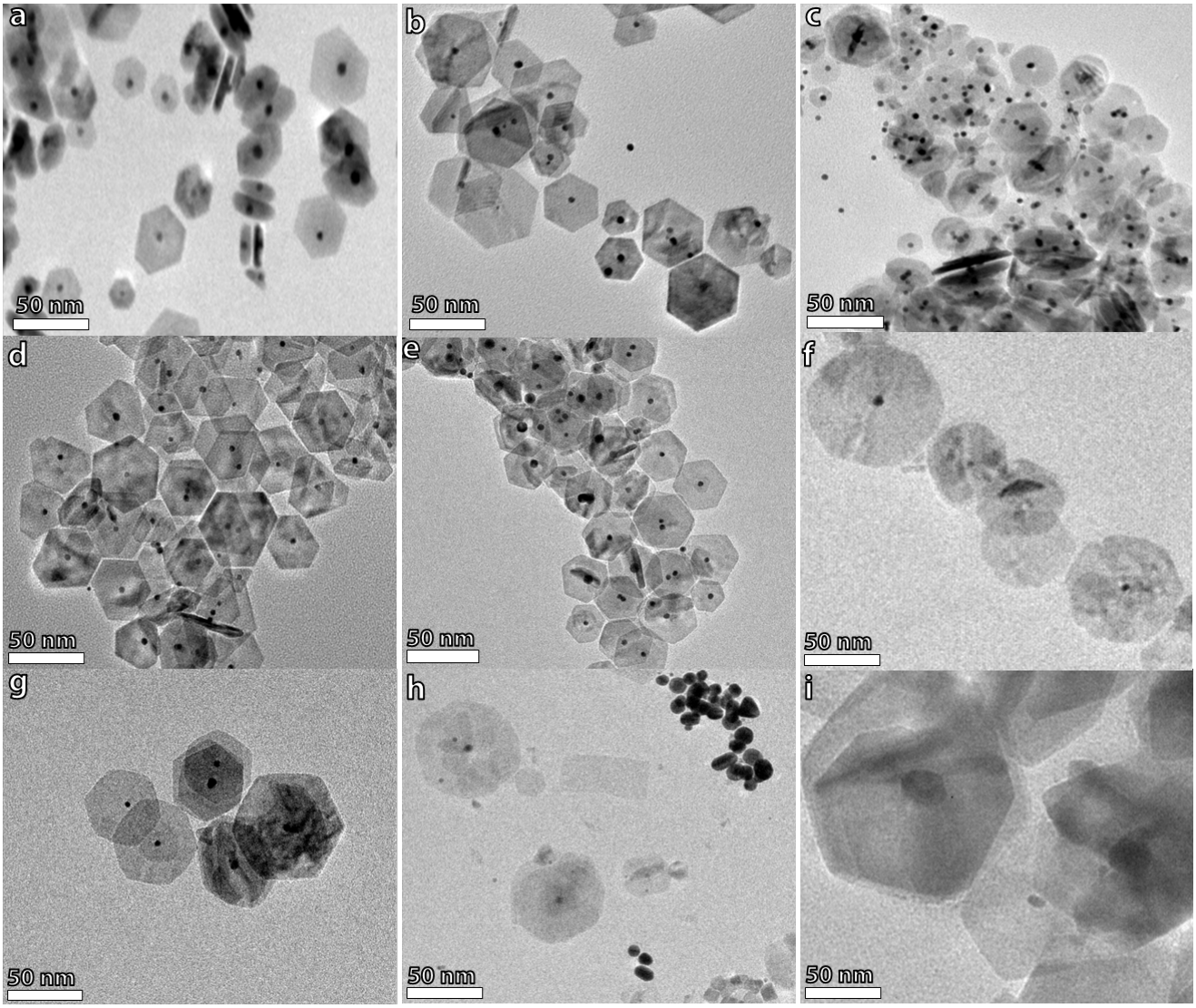

Figure 2: Representative TEM images of the final morphologies of Au-Fe_7S_8 NPLs obtained at different injection temperatures of the seed (Au NPs) (a) 110 °C, (b) 120 °C, (c) 140 °C, (d) 160 °C, (e) 180 °C, (f) 200 °C, (g) 220 °C, (h) 260 °C and (i) 280 °C.

A significant difference was observed in terms of shape, aggregation, surface roughness and how well-developed the hexagonal facets of these NPLs are. It is evident from Figure 2 that the monodisperse and definitive hexagonal-shaped NPLs were observed only at an injection temperature of 160 °C (Figure 2d with its detailed microscopic investigation shown in Figure 3

(a,b). At higher temperatures particularly at 260 and 280 °C, agglomeration of Au NPs seems to be more dominant (Figure 2h, 2i). To investigate it, TGA was performed on the Au NPs seed which revealed its (metal-thiol ligand) decomposition temperature at around 250 °C (Figure S4). So, it can be said that the injection of seed close to its decomposition temperature resulted in the heterogeneous nucleation of Fe_7S_8 on Au seeds leading to the formation of particles with undefined morphology. Also, we think that significant time is required for the seed to provide a suitable crystallographic facet for the growth of Fe_7S_8 on its surface, which is likely to happen only when the seed is injected at a low temperature. Literature suggests that nature of the precursor is another experimental variable that can have a direct impact on the conversion efficiency and morphology of iron sulfide. For example, iron chlorides are not considered an ideal candidate for the formation of iron sulfides due to its high reactivity as compared to $Fe(acac)_3$, even at low temperatures.[32]

By performing several experiments at different seeds injection temperature, it was concluded that the most homogeneous and well-defined hexagonal NPLs (Au-Fe_7S_8) were obtained when Au NPs seeds were injected into the reaction mixture at 160 °C. Therefore, for further investigation this sample was used as a standard. Figure 3 shows the TEM (Figure 3 a) and STEM (Figure 3b) images of Au-Fe_7S_8 NPLs obtained under optimum conditions i.e. Au seed injected at 160 °C.

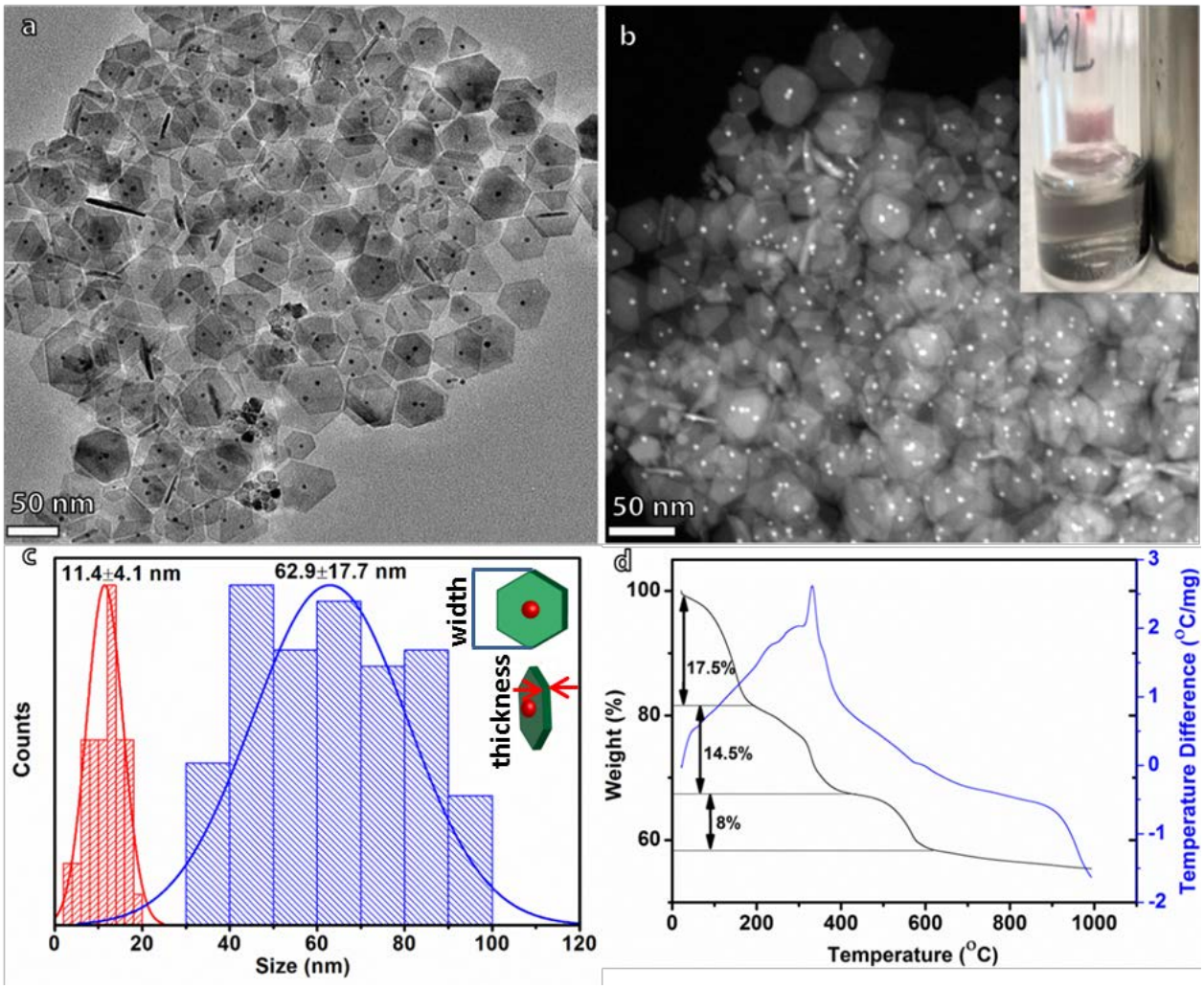

Figure 3: (a) TEM and (b) HAADF-STEM images of Au-Fe_7S_8 NPLs. Inset in (b) showing the response of a sample dispersed in hexane solution to an external magnetic field. (c) sizing histograms of Au-Fe_7S_8 NPLs obtained under optimum reaction conditions with a seed injection temperature of 160 °C. Red columns correspond to the thickness whereas blue columns correspond to the width of the NPLs. Schematics on the top right shows the dimension in which size measurements were done (d) TGA curve for Au-Fe_7S_8 NPLs.

Each NPL presents a well-defined hexagonal-shape with only one Au NP embedded in it. Statistics on the sizes of the heterodimer NPLs show their thickness and width is in the range of

11.4 ±4.1 nm and 62.9±17.7 nm, respectively (Figure 3c), which was further confirmed by AFM as shown in Figure S5. Three major weight losses were observed in the thermogravimetric analysis (TGA)-differential thermal analysis (DTA) curves (Figure 3c). The first mass loss (17.50%) accompanied by small endothermic peaks, occurs from room temperature to 175 °C. This weight loss and the endothermic peak correspond to the loss of the organic solvent. The second weight loss (14.50%) in the temperature range of 175 to 375 °C was attributed to the loss of organic ligands and the third weight loss (8%) in the range of 375-575 °C was also accompanied by some endothermic peaks and this loss can be ascribed to the oxidation of pyrrhotite into iron sulfate.[33] To gain insights into the nature and composition of the intermediate and final product, some parallel structural characterizations were done. Figure 4(a,b) shows two panels of HRTEM images and FFT patterns for Au-Fe_7S_8 NPLs on the aliquots obtained at 260 and 280 °C respectively.

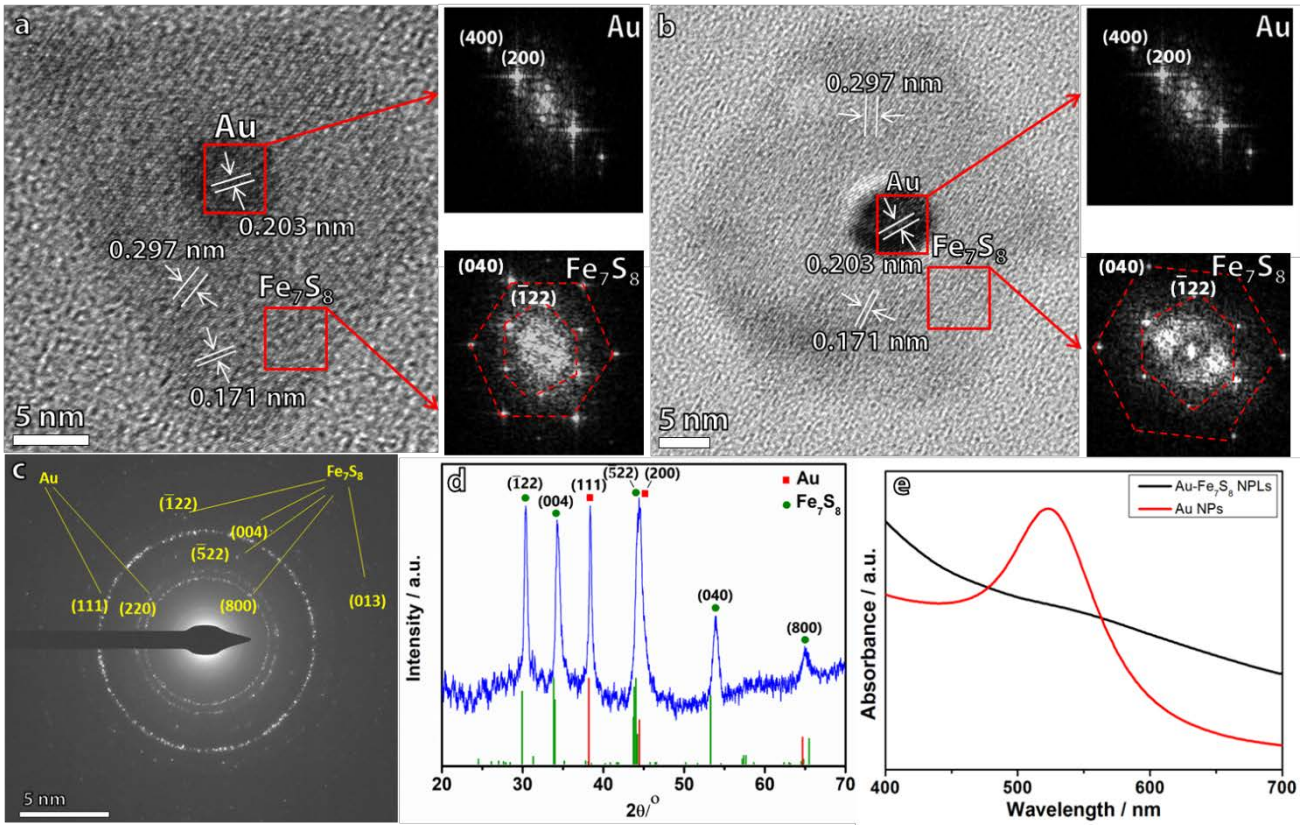

Figure 4: Structural characterizations of the Au-Fe_7S_8 NPLs. (a) HRTEM image of an individual Au-Fe_7S_8 NPLs quenched at an intermediate reaction temperature i.e. 260 °C, with its corresponding FFT patterns represented by red arrows for cubic Au and monoclinic Fe_7S_8 on its right side (b) HRTEM image of an individual Au-Fe_7S_8 NPLs quenched at a final reaction temperature i.e. 280 °C, with its corresponding FFT patterns represented by red arrows for cubic Au and monoclinic Fe_7S_8 on its right side. The lattice fringes highlighted in HRTEM images and its corresponding crystal plane in FFT pattern shows the crystal orientations of the Au and Fe_7S_8. (c) SAED pattern showing distinct diffraction patterns well-indexed to Au and Fe_7S_8 (d) XRD pattern. The standard XRD patterns for cubic Au (red) and monoclinic Fe_7S_8 (green) are provided as a reference at the bottom. (e) UV-Vis absorption spectra of Au NPs and Au-Fe_7S_8 NPLs.

The lattice spacing of the Au NP embedded at the center was found to be 0.203 nm and 0.101 nm, which corresponds to the (200) and (400) planes of Au, respectively. The FFT patterns of Fe_7S_8 from both panels show similar diffraction patterns. Interestingly, interplanar distances of Fe_7S_8 for both panels (left and right) indicated sequential repetition of the $(\bar{1}22)$ of 0.297 nm and (040) of 0.171 nm lattice planes of monoclinic pyrrhotite. These results support the fact that as the reaction proceeds the heterostructures do not undergo phase changes but the morphology changes, which evolved from a truncated triangular to well-defined hexagonal-shaped NPLs. Our experimental results found no evidence for a crystal structure change as reported previously.[34] The co-existence of Au and Fe_7S_8 in the nanoplatelets was further confirmed by the presence of distinct diffraction spots in the SAED of the particles (Figure 4c). The XRD pattern in Figure 4d also displayed two sets of diffraction peaks corresponding with the lattice planes of fcc Au and monoclinic Fe_7S_8 (comparison with other iron sulfides is provided in Figure S6). An apparent overlap of hkl values in the XRD and SAED pattern can be noticed and verifies the formation of the heterodimer. Taking this into account, we believe that along with surface ligand the lattice mismatch also has a significant contribution to the epitaxial growth of Fe_7S_8 on the Au NPs seeds. On the basis of lattice spacings obtained from JCPDS card (29-0723), a mismatch of only 1.61% was determined at the interface of (200) for Au and $(\bar{5}22)$ for Fe_7S_8, a schematic is presented in Figure S7, which further rationalized the heterogeneous nucleation and evolution of Fe_7S_8 into NPLs on the Au NP seeds. Figure 4e shows the absorption spectra of Au (red) and Au-Fe_7S_8 (black) heterodimer which exhibits peak broadening along with a slight red shift. This could be caused by the growth or overlap of Fe_7S_8 NPLs onto the surface of Au NPs resulting in the damping of localized surface plasmon resonance on the Au seeds. To identify the nature and location of individual domains, STEM-EDS was used to construct the elemental maps of the

aliquots taken out at 260 °C (Figures 5a1-e1, S8), which eventually evolved into well-defined hexagonal-shaped NPLs at 280 °C (Figures 5a2-e2, S9).

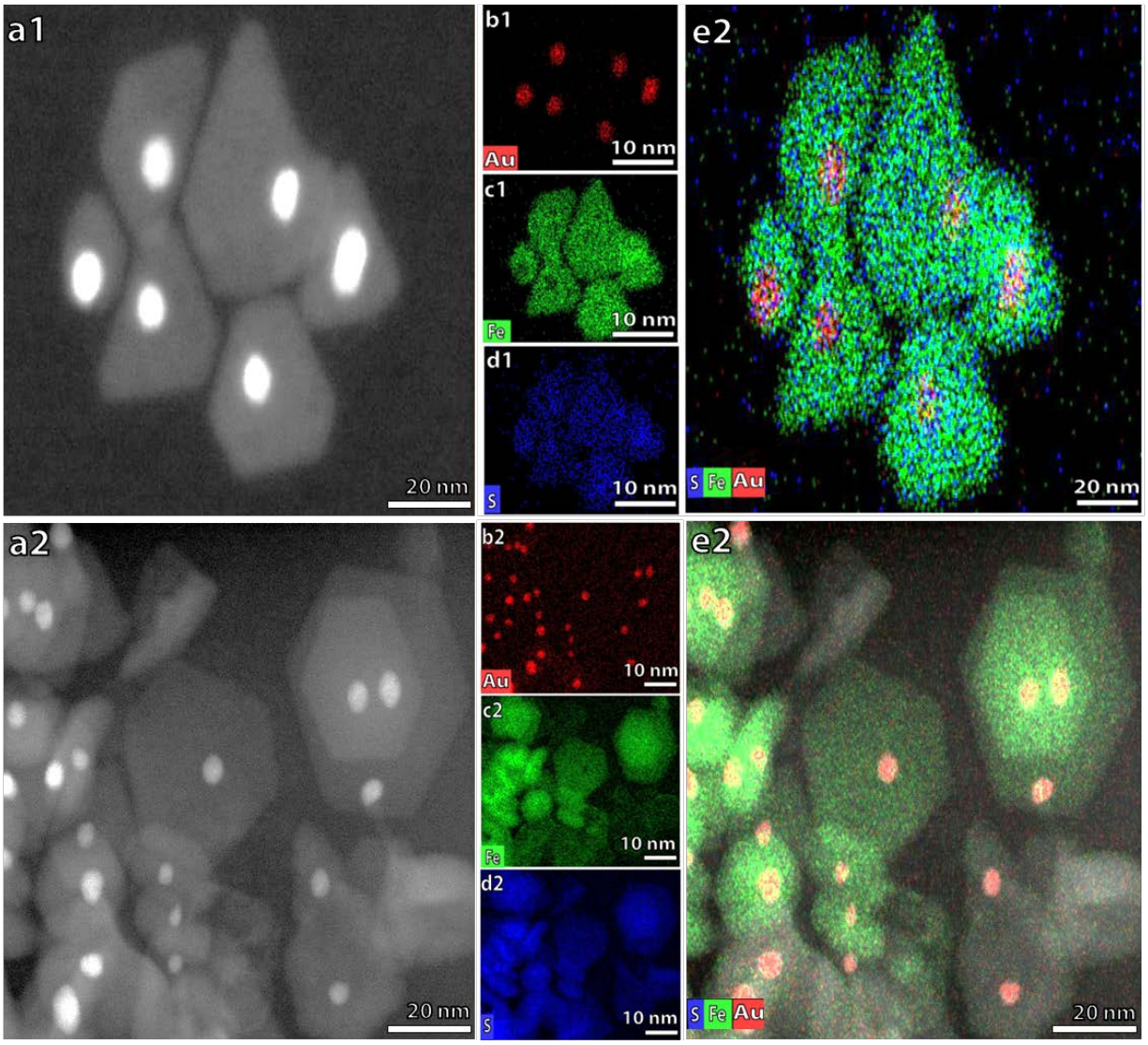

Figure 5: (a1-e1) STEM image and elemental maps of a few Au-Fe_7S_8 NPLs quenched at an intermediate reaction temperature of 260 °C. (a2-e2) STEM image and elemental maps of Au-Fe_7S_8 NPLs quenched at a final reaction temperature of 280 °C.

The elemental mapping provides compelling evidence for the existence of distinctive domains of gold and iron sulfide, thus rationalizing the above mentioned pathway for the formation of

hybrid NPLs (Table S1). So, collectively these observations support the statement that iron sulfide nanoplatelets have grown onto the seed of Au NPs. Apart from the above mentioned pathway, another possible mechanism for the formation of Fe_7S_8 reported in the literature is via pyrite (FeS_2) to greigite (Fe_3S_4) before finally converting into pyrrhotite (Fe_7S_8).[34] In comparison to the iron oxides, the sulfide counterparts are more temperature sensitive towards a phase change. In literature, synthesis of iron sulfide at temperatures below 200 °C produced a mixture of an Fe-S-organic compound and FeS_2. Further increase in temperature i.e. ≥260 °C is enough to facilitate the conversion of FeS_2 into Fe_3S_4 and eventually to Fe_7S_8. This kind of temperature dependent conversion was not observed in this work and only Fe_7S_8 was found as soon as iron sulfide solids formed, as illustrated in Figure 4. This could be attributed to the different synthetic conditions and the use of Au seeds, which prevented homogeneous nucleation.[13, 15, 34-35]

X-ray photoelectron spectroscopy (XPS) was used to examine the bonding environments in the Au-Fe_7S_8 nanoplatelets samples. Notably, the survey spectrum (Figure S10) showed no discernible Au 4f signal associated with the presence of the Au NPs. Given that XPS is a surface sensitive technique - measuring only the top 5-10 nm of a surface – the lack of an Au 4f signal was attributed to the fact that the Au NPs are embedded within the NPLs. The high resolution spectra of the Fe 2p and S 2p core levels are presented in Figure 6 (a).

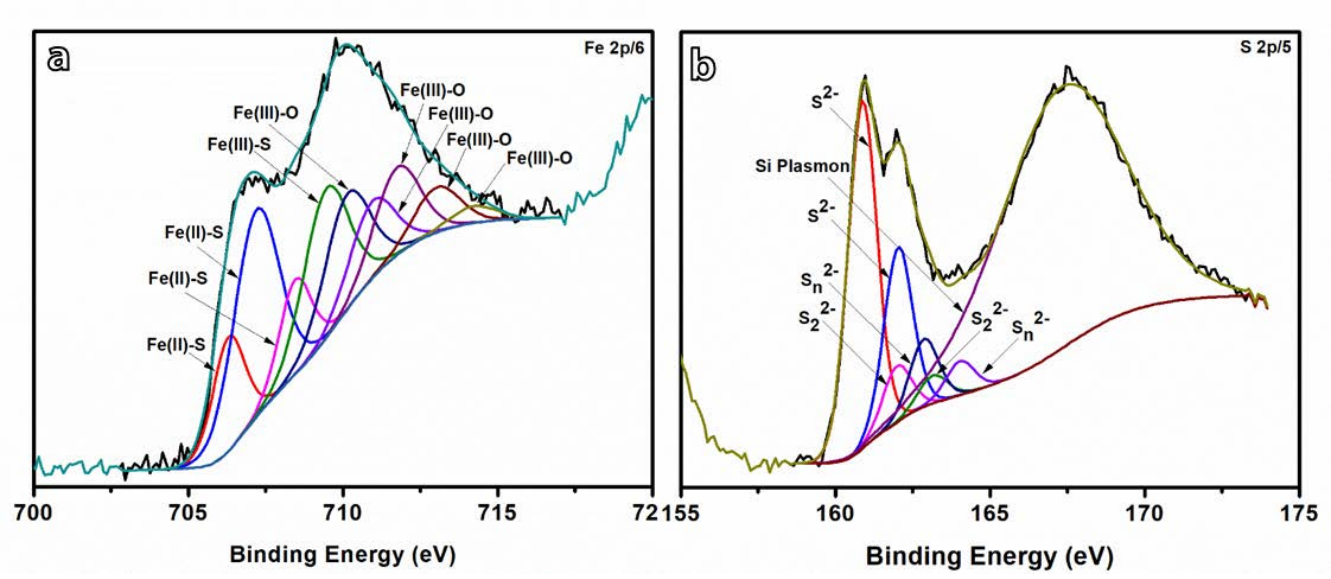

Figure 6: XPS spectra of Au-Fe_7S_8 NPLs (a) Fe and b) S

Deconvolution of the Fe 2p3/2 component provided evidence for the presence of Fe(II)-S, Fe(III)-S and Fe(III)-O bonds, consistent with XPS results from a similar Fe_7S_8 system reported by Han et. al.[15] Specifically, the major Fe(II) component was centered at 707.2 eV, accompanied by the multiplets at 706.3 eV and 708.4 eV. A peak at 709.5 eV was attributed to Fe(III)-S, whilst the remaining peaks at 710.1 eV and 710.9, 711.74, 713.0 and 714.2 eV were assigned to Fe(III)-O (surface oxidation of iron) and the associated multiplets respectively. Using the deconvoluted peak areas of these peaks, a Fe(II):Fe(III) ratio of 2.4 was obtained which is very close to the stoichiometric value of 2.5 for Fe_7S_8. As observed from the deconvoluted S2p spectra (Figure 6 (b)), the spectrum was separated into three main sulfur components, namely monosulfide (S 2p3/2 peak at 160.9 eV), disulfide (162.0eV) and polysulfides (162.87 eV). The major component centered at approximately 167.5 eV was attributed to a Si satellite peak arising from the silicon substrate. Using the proportions of the high resolution Fe 2p and S 2p signals that were attributed to Fe-S bonds (60% and 73%, respectively) and applying it to the relative

atomic concentrations of Fe 2p and S 2s determined from the survey spectrum, the S:Fe ratio attributed to Fe-S bonds is determined to be 1.4. The slight deviation from the stoichiometric ratio of 1.14 was attributed to the different probing depths associated with each of the two elements.[15, 33]

Effect of alkyl chain length of surface ligands on seeds (Au NPs): As mentioned above, DDT capped Au NP seeds can play a crucial role in determining the optimal reaction temperature and the final shape of Au-Fe_7S_8 NPLs which means that other types of thiol ligands immobilized on Au seeds can also support the heterogeneous nucleation of pyrrhotite but may also show different behaviour towards the formation temperature depending on its (metal-thiol ligand) decomposition temperature. To verify this hypothesis, we conducted experiments with other long alkyl chain thiol ligands i.e. hexadecanethiol (HDT) and octadecanethiol (ODT) which have higher boiling points as compared to the DDT.[36] In these experiments, all other reaction parameters were kept constant (see experimental section) except that HDT & ODT capped Au NPs were used as seed and the final reaction temperature was raised to 320 °C due to the higher decomposition temperature of these ligands. Figure S11 and S12 shows the TEM images of aliquots obtained by using HDT and ODT capped Au NPs as a seed. These images illustrate that the initial formation of Au-Fe_7S_8 NPLs occurred at 280 °C when HDT & ODT were used and the final NPLs remained stable to up to 320 °C unlike the NPLs with DDT capped Au NPs seeds where the formation and final temperature range for Au-Fe_7S_8 was quite low i.e. 260-280 °C (Figure 1). Comparison of all three products obtained from the different thiol capped Au NP seeds, i.e. DDT, HDT and ODT, it is quite evident that the stability of hexagonal shaped NPLs increases with increasing alkyl chain length. This in turn is due to the increase in boiling points[36] with increase in the alkyl chain length (C12-C18).

Effect of ligand on the surface of seed (OL-Am Au NPs). To test the impact of ligand, we switched to oleylamine (OL-Am) capped Au NPs[37], which were then subjected to ligand exchange with DDT. Addition of only 259 μL of DDT instantly turned deep red Au NPs into a purple coloured solution which were then used as seed for the synthesis of NPLs under above mentioned optimum conditions. Figure S2 represents the TEM images of the heterodimer obtained from this method. Although the hexagonal morphology of Fe_7S_8 was still retained the significant contribution of Au NPs in making of this structure is significantly lost. Unlike the previous method, herein we observed a random distribution of Au NPs within NPLs which ranged from none at all to more than one. Apart from that, the thickness of the NPLs was also affected and much thicker NPLs were obtained as shown in Figure S2 (a). To highlight the influence of the surface ligand on the shape and thickness of NPLs, we then used elemental sulfur as an alternate source of sulfur rather than DDT. A homogeneous solution of OL-Am capped Au NPs was prepared in 0.1 M sulfur solution followed by its injection into the iron precursor solution. TEM images shown in Figure S13 revealed the formation of a distorted hexagonal-shaped heterodimer of Au-Fe_7S_8 along with some homogeneously nucleated iron sulfide.

Altogether, these observations enlighten us with subtle but yet important aspects of the synthesis framework which can significantly alter the final morphology and formation temperature (Figure S11-S13) of the heterodimer (Table S2).

Electrocatalytic hydrogen evolution reaction (HER) Performance of Au-Fe_7S_8. The electrocatalytic activity of Au-Fe_7S_8 towards the HER was measured at room temperature in an alkaline electrolyte (1.0 M KOH). The electrocatalyst, Au-Fe_7S_8, was supported on a glassy carbon electrode to be employed as a working electrode in a three-electrode electrochemical

setup. The results obtained in the form of a polarization curve (Figure 7) showed much better electrocatalytic behaviour as compared to the bare Glassy Carbon (GC) electrode. The hydrogen evolution by the electrocatalyst was observed to be initiated at over-potential of 265 mV (defined as the potential required obtaining a current density of 1.0 mA cm^{-2}) which is significantly lower than the bare GC electrode. Another comparison is with respect to the overpotential required to deliver a 10 mA cm^{-2} current density. This represents a metric relevant to solar fuels synthesis[38] and also supports the greatly enhanced capability of Au-Fe_7S_8 in catalysing the HER compared to bare GC (376 versus 702 mV). In addition to the reduced overpotential, the Au-Fe_7S_8-modified GC electrode gave a lower Tafel slope relative to the bare GC i.e. 111 versus 208 mV $decade^{-1}$ (Figure 7, b), suggesting that the reaction kinetics of catalysis in generating hydrogen is more favourable[39] with density functional theory (DFT) configuration presented in Figure S14. Given a small Tafel slope, HER on the catalyst containing electrode is expected to occur rapidly upon a moderate rise in overpotential which is beneficial for practical electrochemical devices. Many other forms of iron sulfide, including pyrrhotite have shown great potential for HER[40] and believe this can be improved in future by incorporating other conductive materials or by focusing on the parameters that can expose more active iron sites for catalysis.[41-43]

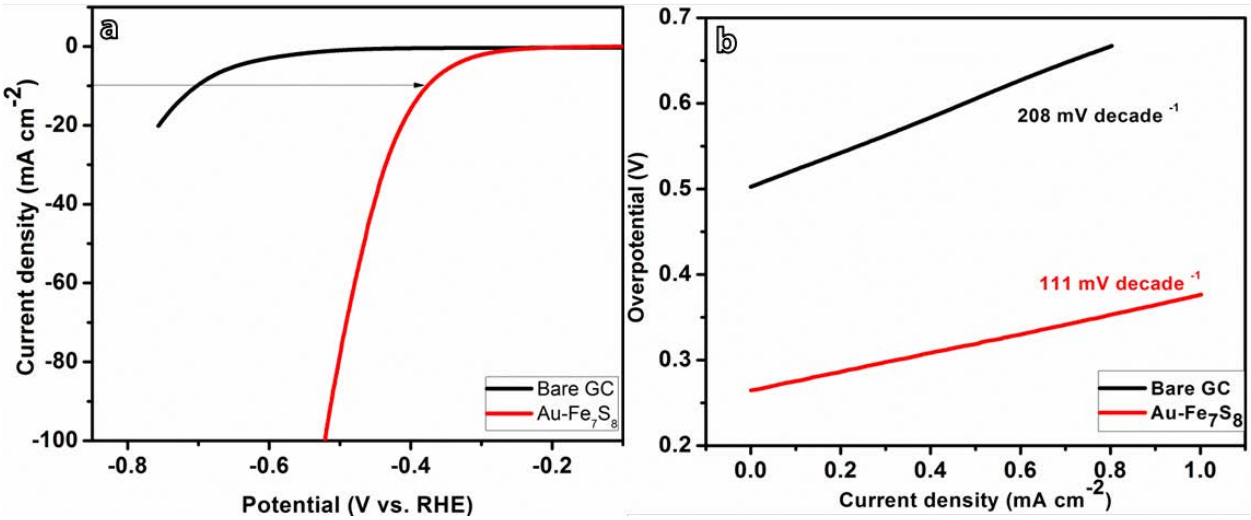

Figure 7: a) Polarization curves of the Au-Fe_7S_8-modified GC electrode and the bare GC electrode. b) Corresponding Tafel plots of the Au-Fe_7S_8-modified GC electrode and the bare GC electrode.

Ag/Ag_2S-Fe_7S_8. A similar seed mediated growth strategy was adopted for the synthesis of a hybrid heterodimer of Ag-Fe_7S_8 under the experimental conditions, which were optimized for Au-Fe_7S_8. To keep reaction parameters identical, only spherical thiol capped Ag NPs were used as seeds.[28] Figure S15 presents TEM, HRTEM and FFT pattern for the Ag_2S-Fe_7S_8 heterodimer and Figure S16 represents the TEM, STEM and elemental mapping images of the isolated particle of Ag_2S-Fe_7S_8 that was quenched at 260 °C (S16, a1-e1) and 280 °C (S16, a2-d2) respectively.

CONCLUSION

In conclusion, we have developed a facile method for the synthesis of noble metal and pyrrhotite (Au-Fe_7S_8 and Ag_2S-Fe_7S_8) NPLs, for the first time, through a well-established seeded growth approach. These NPLs were found to be crucially dependent on the surface binding ligand (-

thiol) on the noble metal seed and resulted in particles that were homogeneous in size, thickness and in containing one Au seed per particle. A low injection temperature of seed was found to be correlated to the shape and thickness of NPLs and is an effective way to control the synthesis. The obtained Au-Fe_7S_8 nanoplatelets have been used as an electrocatalyst for HER and displayed positive results. We believe that it can be improved in future by focusing on the parameters that can expose more active iron sites for catalysis. Thus, with the formation of these noble metal – magnetic iron sulfide NPLs we have broadened the chemical 'palette' that can be incorporated into nanoparticle heterodimers.

Supporting Information. The Supporting Information includes detailed experimental conditions for XPS and TGA were performed. Additional sample characterization for Au-Fe_7S_8 is provided in terms of TEM images, size distribution curve at different temperatures, TGA curve for Au seeds, AFM, XRD pattern for comparison with other standard iron sulfides, crystallographic relation between gold and iron pyrrhotite in terms of structural model, EDS and XPS survey spectra and TEM images of NPLs synthesized with HDT and ODT capped Au NPs. The experimental details for the catalytic potential of Au-Fe_7S_8 is also explained in terms of the hydrogen evolution reaction (HER) along with density functional theory (DFT) simulation details. The STEM, elemental mapping, FFT pattern and TEM images for Ag_2S-Fe_7S_8 are also provided along with a brief description. Tables S1 to S3 are given for the better understanding of atomic percentage via EDS analysis, detailed experimental conditions and Gibbs-Free energy values respectively.

Corresponding Author

* guohua.jia@curtin.edu.au ； F.Jones@curtin.edu.au

ACKNOWLEDGMENT

This work was supported by Australian Research Council (ARC) Discovery Early Career Researcher Award (DECRA) (Project ID: DE160100589). S.J. would like to thank Curtin strategic international research scholarship (CSIRS). This research was undertaken using the facilities (TEM, XRD and XPS) at the John de Laeter Centre, Curtin University. The authors acknowledge the use of equipment, scientific and technical assistance of the WA X-ray Surface Analysis Facility, funded by the Australian Research Council LIEF grant LE120100026. The authors also acknowledge the facilities, and the scientific and technical assistance of the Australian Microscopy & Microanalysis Research Facility at the Centre for Microscopy, Characterization & Analysis, The University of Western Australia, a facility funded by the University, State and Commonwealth Governments.

REFERENCES

1. Schaak, R. E.; Williams, M. E. Full Disclosure: The Practical Side of Nanoscale Total Synthesis. *ACS Nano* **2012**, *6*, 8492-8497.

2. Fenton, J. L.; Hodges, J. M.; Schaak, R. E. Synthetic Deconvolution of Interfaces and Materials Components in Hybrid Nanoparticles. *Chem. Mater.* **2017**, *29*, 6168-6177.

3. Leung, K. C.-F.; Xuan, S.; Zhu, X.; Wang, D.; Chak, C.-P.; Lee, S.-F.; Ho, W. K. W.; Chung, B. C. T. Gold and Iron Oxide Hybrid Nanocomposite Materials. *Chem. Soc. Rev.* **2012**, *41*, 1911-1928.

4. Jiang, M.; Liu, W.; Yang, X.; Jiang, Z.; Yao, T.; Wei, S.; Peng, X. Pt/Fe_3O_4 Core/Shell Triangular Nanoprisms by Heteroepitaxy: Facet Selectivity at the Pt–Fe_3O_4 Interface and the Fe_3O_4 Outer Surface. *ACS Nano* **2015**, *9*, 10950-10960.

5. Shi, W.; Zeng, H.; Sahoo, Y.; Ohulchanskyy, T. Y.; Ding, Y.; Wang, Z. L.; Swihart, M.; Prasad, P. N. A General Approach to Binary and Ternary Hybrid Nanocrystals. *Nano Lett.* **2006**, *6*, 875-881.

6. Shan, G.; Zhong, M.; Wang, S.; Li, Y.; Liu, Y. The Synthesis and Optical Properties of the Heterostructured ZnO/Au Nanocomposites. *J. Colloid Interface Sci.* **2008**, *326*, 392-395.

7. Wang, C.; Yin, H.; Dai, S.; Sun, S. A General Approach to Noble Metal−Metal Oxide Dumbbell Nanoparticles and Their Catalytic Application for CO Oxidation. *Chem. Mater.* **2010**, *22*, 3277-3282.

8. Li, P.; Wei, Z.; Wu, T.; Peng, Q.; Li, Y. Au−ZnO Hybrid Nanopyramids and Their Photocatalytic Properties. *J. Am. Chem. Soc.* **2011**, *133*, 5660-5663.

9. Stefan, M.; Leostean, C.; Pana, O.; Soran, M. L.; Suciu, R. C.; Gautron, E.; Chauvet, O. Synthesis and Characterization of Fe_3O_4@ZnS and Fe_3O_4@Au@ZnS Core–Shell Nanoparticles. *Appl. Surf. Sci.* **2014**, *288*, 180-192.

10. Zhao, H; Zhang, H.; Cui, G.; Dong, Y.; Wang, G.; Jiang, P.; Wu, X.; Zhao, N. A Photochemical Synthesis Route to Typical Transition Metal Sulfides as Highly Effeicient Cocatalyst for Hydrogen Evolution: from the case of NiS/G-C_3N_4. *Appl. Catal. B Environ.* **2018**, *225*, 284-290.

11. Zhu, X., Liu, D.; Zheng, D.; Wang, G.; Huang, X.; Harris, J.; Qu, D.; Qu, D. Dual Carbon-Protected Metal Sulfides and their Application to Sodium-Ion Battery Anodes, *J. Mater. Chem. A*, **2018**, *6*, 13294-13301.

12. Liu, W.; Niu, H.; Yang, J.; Cheng, K.; Ye, K.; Zhu, K.; Wang, G.; Cao, D.; Yan, J. Ternary Transition Metal Sulfides Embedded in Graphene Nanosheets as Both the Anode and Cathode for High-Performance Asymmetric Supercapacitors. *Chem. Mater.* **2018**, *30*, 1055-1068.

13. Liu, H. F.; Huang, A.; Chi, D. Z. Thermal Annealing of Nanocrystalline Fe_3S_4 Films Deposited on Si Substrates by DC-Magnetron Sputtering at Room Temperature. *J. Phys. D: Appl. Phys.* **2010**, *43*, 455405.

14. Shimizu, R.; Yamada, Y.; Kobayashi, Y. Liquid Phase Synthesis of Iron Sulfide Particles. *J. Radioanal. Nucl. Ch.* **2015**, *303*, 1473-1476.

15. Han, W.; Gao, M. Investigations on Iron Sulfide Nanosheets Prepared via a Single-Source Precursor Approach. *Cryst. Growth Des.* **2008**, *8*, 1023-1030.

16. Wu, M.; Tse, J. S.; Pan, Y. Electronic Structures of Greigite (Fe_3S_4): A Hybrid Functional Study and Prediction for a Verwey Transition. *Sci. Rep.* **2016**, *6*, 21637.

17. Beal, J. H. L.; Etchegoin, P. G.; Tilley, R. D. Synthesis and Characterisation of Magnetic Iron Sulfide Nanocrystals. *J. Solid State Chem.* **2012**, *189*, 57-62.

18. Chen, S.; Kang, Z.; Zhang, X.; Xie, J.; Wang, H.; Shao, W.; Zheng, X.; Yan, W.; Pan, B.; Xie, Y. Highly Active Fe Sites in Ultrathin Pyrrhotite Fe_7S_8 Nanosheets Realizing Efficient Electrocatalytic Oxygen Evolution. *ACS Cent. Sci.* **2017**, *3*, 1221-1227.

19. Veerasubramani, G. K.; Park, M.-S.; Choi, J.-Y.; Lee, Y.-S.; Kim, S. J.; Kim, D.-W. Rational combination of an alabandite MnS Laminated pyrrhotite Fe1-x S Nanocomposite as a superior anode material for high performance sodium-ion battery. *ACS Sustainable Chem. Eng*. **2019**, DOI: 10.1021/acssuschemeng.8b05904.

20. Zhang, K.; Chen, F.; Pan, H.; Wang, L., Wang, D.; Jiang, Y.; Wang, L.; Qian, Y. Study on the Effect of Transition Metal Sulfide in Lithium-Sulfur Battery. *Inorg. Chem. Front.* **2019**, *6*, 477-481.

22. Barman, D.; Ghosh, S.; Paul, S.; Dalal, B.; De, S. K. Cation Exchange Mediated Synthesis of Library of Plasmomagnetic Nanoheterostrucutres Transformation of 2-Dimenssional-Shaped Fe_7S_8 Nanoplatelets to Cu-Fe-S-Based Ternary Compound. *Chem. Mater.* **2018**, *30*, 5550-5560.

23. Read, C. G.; Biacchi, A. J.; Schaak, R. E. Au–Ge and Ag–Ge Heterodimers with Tunable Domain Sizes: A Supersaturation-Precipitation Route to Colloidal Hybrid Nanoparticles. *Chem. Mater.* **2013**, *25*, 4304-4311.

24. Bradley, M. J.; Biacchi, A. J.; Schaak, R. E. Chemical Transformation of Pt–Fe_3O_4 Colloidal Hybrid Nanoparticles into PtPb–Fe_3O_4 and Pt_3Sn–Fe_3O_4 Heterodimers and (PtPb–Fe_3O_4)n Nanoflowers. *Chem. Mater.* **2013**, *25*, 1886-1892.

25. Buck, M. R.; Bondi, J. F.; Schaak, R. E. A Total-Synthesis Framework for the Construction of High-Order Colloidal Hybrid Nanoparticles. *Nat. Chem.* **2012**, *4*, 37-44.

26. Hodges, J. M.; Morse, J. R.; Fenton, J. L.; Ackerman, J. D.; Alameda, L. T.; Schaak, R. E. Insights into the Seeded-Growth Synthesis of Colloidal Hybrid Nanoparticles. *Chem. Mater.* **2017**, *29*, 106-119.

27. Gordon, T. R.; Schaak, R. E. Synthesis of Hybrid Au-In_2O_3 Nanoparticles Exhibiting Dual Plasmonic Resonance. *Chem. Mater.* **2014**, *26*, 5900-5904.

28. Hodges, J. M.; Biacchi, A. J.; Schaak, R. E. Ternary Hybrid Nanoparticle Isomers: Directing the Nucleation of Ag on Pt–Fe_3O_4 Using a Solid-State Protecting Group. *ACS Nano* **2014**, *8*, 1047-1055.

29. Bradley, M. J.; Read, C. G.; Schaak, R. E. Pt–Au Nanoparticle Heterodimers as Seeds for Pt–Au–Metal Sulfide Heterotrimers: Thermal Stability and Chemoselective Growth Characteristics. *J. Phys. Chem. C* **2015**, *119*, 8952-8959.

30. Brust, M.; Walker, M.; Bethell, D.; Schiffrin, D. J.; Whyman, R. Synthesis of Thiol-Derivatised Gold Nanoparticles in a Two-Phase Liquid-Liquid System. *J. Chem. Soc., Chem. Commun.* **1994**, *0*, 801-802.

31. Vanegas, J. P.; Scaiano, J. C.; Lanterna, A. E.; Thiol-Stabilized Gold Nanoparticles: New Ways to Displace Thiol Layers Using Yttrium or Lanthanide Chlorides. *Langmuir*. **2017**, *33*, 12149-12154.

32. Li, T.; Li, H.; Wu, Z.; Hao, H.; Liu, J.; Huang, T.; Sun, H.; Zhang, J.; Zhang, H.; Guo, Z. Colloidal Synthesis of Greigite Nanoplates with Controlled Lateral Size for Electrochemical Applications. *Nanoscale* **2015**, *7*, 4171-4178.

33. Zhang, K.; Zhang, T.; Liang, J.; Zhu, Y.; Lin, N.; Qian, Y. A Potential Pyrrhotite (Fe_7S_8) Anode Material for Lithium Storage. *RSC Adv.* **2015**, *5*, 14828-14831.

34. Yuan, B. X.; Fu, H. H.; Luan, W. L. One-Step Synthesis of Fe_3S_4 Micro-Crystals and its Facile Transformation to Fe_7S_8 Micro-Crystals. *Appl. Mech. Mater.* **2012**, *130-134*, 1270-1275.

35. Abdelhady, A. L.; Malik, M. A.; O'Brien, P.; Tuna, F. Nickel and Iron Sulfide Nanoparticles from Thiobiurets. *J. Phys. Chem. C* **2012**, *116*, 2253-2259.

36. Zhang, P.; Chu, A. Y.-C.; Sham, T.-K.; Yao, Y.; Lee, S.-T. Chemical Synthesis and Structural Studies of Thiol-Capped Gold Nanoparticles. *Can. J. Chem*. **2009**, *87*, 335-340.

37. Hiramatsu, H.; Osterloh, F. E. A Simple Large-Scale Synthesis of Nearly Monodisperse Gold and Silver Nanoparticles with Adjustable Sizes and with Exchangeable Surfactants. *Chem. Mater.* **2004**, *16*, 2509-2511.

38. Benck, J. D.; Hellstern, T. R.; Kibsgaard, J.; Chakthranont, P.; Jaramillo, T. F. Catalyzing the Hydrogen Evolution Reaction (HER) with Molybdenum Sulfide Nanomaterials. *ACS Catal.* **2014**, *4*, 3957-3971.

39. Xu, X.; Chen, Y.; Zhou, W.; Zhu, Z.; Su, C.; Liu, M.; Shao, Z. A Perovskite Electrocatalyst for Efficient Hydrogen Evolution Reaction. *Adv. Mater.* **2016**, *28*, 6442-6448.

40. Chen, S.; Kang, Z.; Zhang, X.; Xie, J., Wang, H.; Shao, W.; Zheng, Z.; Yan, W.; Pan, B.; Xie, Y. Highly Actice Fe Sites in Ultrathin Pyrrhotite Fe_7S_8 Nanosheets Realizing Efficient Electrocatalytic Oxygen Evolution. *ACS Cent. Sci.* **2017**, *3*, 1221-1227.

41. Shi, L.; Li, D.; Yu. J., Liu, H.; Zhao, Y.; Xin, H.; Lin, Y.; Lin, C.; Li, C.; Zhu, C. Uniform Core-Shell Nanobiscuits of Fe_7S_8@C for Lithium-Ion and Sodium-Ion Batteries with Excellent Performance. *J. Mater. Chem. A* **2018**, *6*, 7967-7976.

42. Chen, D.; Zhang, H.; Li, Y.; Pang, Y.; Yin, Z.; Sun, H.; Zhang, L.-C.; Wang, S.; Saunder, M.; Barker, E.; et al. Spontaneous Formation of Noble-and Heavy-Metal-Free Alloyed Semiconductor Quantum Rods for Efficient Photocatalysis. *Adv. Mater.* **2018**, *1803351*, 1-10.

43. Jia, G.; Pang, Y.; Ning, J.; Banin, U.; Ji, B. Heavy-Metal Free Colloidal Semiconductor Nanorods: Recent Advances and Future Perspectives. *Adv. Mater.* **2019**, DOI: 10.1002/adma.201900781.

TOC Graphic